# Adaptive Multi-Parameter Model-Free Delay Compensation in Damping Impedance Interfaced Distributed Power System Co-Simulation

Elutunji Buraimoh, *Member, IEEE*, Gokhan Ozkan, *Senior Member, IEEE*, Laxman Timilsina, *Member, IEEE*, Grace Muriithi, *Graduate Student Member, IEEE*, Ali Moghassemi, *Graduate Student Member, IEEE*, Ali Arsalan, *Graduate Student Member, IEEE*, SM Imrat Rahman, *Graduate Student Member, IEEE*, Behnaz Papari, *Senior Member, IEEE*, Mustafa Ozden, *Member, IEEE*, and Christopher Edrington, *Senior Member, IEEE*

***Abstract*—Virtual integration of geographically dispersed laboratories through real-time co-simulation presents powerful capabilities for co-simulating massive complex systems but it is hindered by communication delays that compromise accuracy and stability. This challenge is particularly concerning for real-time power system co-simulation, where delays can induce synchronization loss and limit dynamic and transient studies. This study proposes an adaptive, multi-parameter model-free framework for predicting and compensating delays in co-simulated systems, addressing this critical issue. This framework leverages the improved damping impedance method interface algorithm and an adaptive, parameter-tuning predictor system that predicts and compensates for delays without requiring complex interface signal transformation, processing, decomposition, reconstruction, phase estimation, system models, and no human interference. The proposed approach is validated using a joint experiment between two laboratories at Clemson, SC, USA and Greenville, SC, USA, with the Damping Impedance Method as an Interface Algorithm between the two partitioned subsystems. The coupling errors, state tracking errors, and residual complex power are used as evaluation metrics for the proposed delay compensation. This approach enhances co-simulation accuracy and stability, facilitating reliable dynamic and transient analyses.**

***Index Terms*—Co-simulation, damping impedance method, delay, delay prediction, interface algorithms, interface signals.**

## I. Introduction

GEOGRAPHICALLY distributed real-time co-simulation (GDRTCS), leveraging Hardware-in-the-Loop (HIL), Power Hardware-in-the-Loop (PHIL), and Controller Hardware-in-the-Loop (CHIL) techniques, enables geographically dispersed simulators to function as a unified computational system. Widely applied in power systems [1], aerospace, and automotive engineering, GDRTCS facilitates the simulation of complex systems under diverse conditions, reducing the reliance on physical prototypes and expensive testing facilities [2]. In power systems, which encompass generation, transmission, and distribution networks integrated with renewable resources and control mechanisms, GDRTCS allows for comprehensive testing and validation while addressing operational, economic, and regulatory challenges [3], [4]. By integrating physical hardware with computational models, HIL simulations—comprising CHIL for control algorithm validation and PHIL for testing power equipment—support performance optimization and real-time assessment [5], [6]. Using high-bandwidth communication networks [7] and precise synchronization protocols [8], GDRTCS enhances productivity, promotes cross-geographical collaboration [9], [10], and creates realistic testing environments, ultimately improving safety, efficiency, and performance across industries [11], [12].

The surge in research on GDRTCS, integrating geographically dispersed software and hardware, has revealed critical challenges, with communication latency as a primary issue [7], [9]. Latency, the delay between transmitting signals and numerical integration [13], can destabilize networked co-simulations, especially in power systems sensitive to delays, risking synchronization loss and reduced fidelity. High-bandwidth, low-latency networks [8] and advanced synchronization algorithms [14] are essential to ensure consistent results. Despite these challenges of latency, real-time simulator integration has become increasingly prevalent [15], [16], supported by advancements in HIL techniques and the growing need for flexible, scalable, and distributed testing environments [17], [18]. To mitigate communication latency challenges, various solutions have been proposed, including the use of fiber-optic communication networks, precise clock synchronization techniques, parallel processing architectures, predictive compensation algorithms, and specialized co-simulation frameworks [7], [19]. These

Received 16 August 2024; revised 15 January 2025 and 11 May 2025; accepted 30 May 2025. Date of publication 2 June 2025; date of current version 22 October 2025. This work was supported by the Clemson University's Virtual Prototyping of Autonomy Enabled Ground Systems (VIPR-GS) under Cooperative Agreement number W56HZV-21-2-0001 with the US Army DEVCOM Ground Vehicle Systems Center (GVSC). Paper no. TPWRS-01299-2024.
*(Corresponding author: Elutunji Buraimoh.)*

Elutunji Buraimoh, Gokhan Ozkan, Laxman Timilsina, Ali Moghassemi, SM Imrat Rahman, Mustafa Ozden, and Christopher Edrington are with the Holcombe Department of Electrical and Computer Engineering, Clemson University, Clemson, SC 29634 USA (e-mail: eburaim@clemson.edu).

Grace Muriithi, Ali Arsalan, and Behnaz Papari are with the Department of Automotive Engineering, Clemson University, Clemson, SC 29634 USA.
Color versions of one or more figures in this article are available at https://doi.org/10.1109/TPWRS.2025.3575793.

Digital Object Identifier 10.1109/TPWRS.2025.3575793

advancements drive the adoption of real-time co-simulation, enabling accurate, stable dynamic analyses for complex systems like power grids [10], [20].

Handling and computation of interface signals are pivotal in GDRTCS, as the signals undergo transformation and reconstruction at both local and remote locations. This transformation addresses communication delays and mitigates their effects using delay compensation techniques [2], [21]. GDRTCS Interface Algorithms (IAs) process these signals as slowly varying quantities to overcome challenges such as time-varying delays, packet loss, and reordering inherent in shared communication networks. The transformation process include Root Mean Square (RMS), Dynamic Phasors (DPs), Synchronous Reference Frames (SRF), and Wave Variable (WV) transformation involves converting voltage and current waveforms into slowly varying equivalents at the sending end, transmitting these signals across the network, and reconstructing them into their original time-varying forms at the receiving end [8], [9]. These reconstructed signals are then utilized by the controlled source of the IAs to simulate the behavior of the remote subsystem locally. This approach, comprising signal transformation, network transmission, reconstruction, and IA integration, ensures that the fidelity and stability of signals are preserved in GDRTCS, enabling accurate and stable co-simulation of power systems despite the challenges posed by GDRTCS. However, these methods struggle to maintain fidelity during transients [22].

The RMS, frequency, and phase angle method is a fundamental approach for representing interface quantities in GDRTCS. It decomposes interface signals into RMS value, frequency, and phase angle, enabling accurate data exchange between simulators [21], [22] and reconstruction of time-domain signals at the receiving end, ensuring fidelity and stability. This method is widely used in GDRTCS. For example, it was employed to integrate an IEEE 14-bus system on a Real Time Digital Simulator (RTDS) platform at Idaho National Laboratory (INL) with a wind turbine model at the National Renewable Energy Laboratory (NREL) [23]. Similarly, a modified IEEE 13-bus system simulated in Real Time Digital Simulator Computer Aided Design (RSCAD) was interfaced with hardware under test using this technique [24].

DPs are co-simulation tools that use time-varying Fourier quantities to model and analyze power systems, particularly useful for capturing dynamic state changes in grids with increasing power electronics integration. The Dynamic Phasor approach enables efficient simulation of larger grids with relatively low computational costs of Electromagnetic Transient (EMT) simulations [2], [25]. By approximating complex time-domain waveforms using Fourier series, DPs handle non-stationary situations in power systems [12], [26]. In GDRTCS, DP coefficients are transmitted to remote simulators, where time-domain signals are reconstructed. This method mitigates delays, integrates frequency into signals, and supports co-simulation of subsystems in different domains [27]. For instance, [22] demonstrates partitioning a power system into subsystems, where DPs simulate less transient-sensitive sections while EMT captures fast transients caused by power-electronic switches. Combining DP and EMT simulations offers detailed yet computationally efficient power system modeling, particularly for areas where fast transients are negligible or computational efficiency is crucial [22], [28]. In a stability comparison of RMS and DP methods for GDRTCS in [21], the DP approach demonstrated greater stability, improving accuracy, especially under non-stationary conditions, though it involves higher computational complexity.

The SRF interface addresses the shortcomings of phasor-based interfaces in GDRTCS [29]. While RMS and DP are commonly used for exchanging interface signals, they have limitations such as reduced fidelity during transients, phase shifts, and high computational complexity [30], [31]. To overcome these drawbacks, the SRF interface integrates traditional transformations into the IA to facilitate GDRTCS, applicable to real-time co-simulation and PHIL setups [29]. By transforming time-domain signals into a synchronous reference frame [32], the SRF interface makes them suitable for packet-based transmission and compensates for time delays. Comparative evaluations show that the SRF interface outperforms DP methods in fidelity, delay compensation, and computational efficiency [33]. For example, [29] demonstrates its effectiveness in partitioning power systems into subsystems, where it handles signals with higher accuracy during dynamic conditions compared to traditional methods. The SRF interface represents a significant improvement for GDRTCS by addressing time delays and synchronization challenges, simplifying computational processes, and enabling high-fidelity real-time co-simulation across geographically dispersed systems [22], [28].

To address time delays, WV Transformations are employed, replacing direct power transfer with wave-based communication to ensure stability during delays. This approach stabilizes GDRTCS under conditions that destabilize traditional Ideal Transformer Models (ITM) [28]. Wave variable-based methods transform interface signals to enhance stability and accuracy under small communication delays; however, their performance under larger delays depends on the development of improved interface algorithms [1], [7], [28]. In High-Voltage Direct Current (HVDC) simulations, Wave Variable Transformations maintain stability where ITM fails, and integration with dynamic phasors enhances IA fidelity and stability. GDRTCS divides large networks into subsystems, using interface techniques like RMS, dynamic phasors, or SRF transformations to ensure precise real-time data exchange [34], with communication interfaces managing data conversion and synchronization for stability in distributed simulations.

The selection of IA is critical in GDRTCS, as it directly impacts simulation accuracy, computational speed, and system stability [5]. Many existing algorithms employ advanced signal processing techniques—such as signal decomposition and reconstruction—to mitigate the effects of communication delays [25], [35]. These methods exhibit a slow response speed due to their inherent windowing characteristics, which can constrain their ability to accurately reproduce faster transients, such as phase shifts. [7]. Also, the high computational complexity associated with their implementation is a significant shortcoming. Lastly, these methods limit applicability to non-power systems and non-alternating current variables. To mitigate the challenge of increased computational complexity on resource-constrained distributed Real-Time Simulators, the deployment of an external Field-Programmable Gate Array (FPGA) node dedicated to these decomposition and exchange was proposed in literature [7], [36]. However, this approach introduces additional costs due to the inclusion of the FPGA node and may incur increased delays resulting from the additional interface requirements between the real-time simulator and the FPGA node. Minimizing communication latency is particularly crucial in power systems, where time synchronization and high-fidelity simulations are essential for dynamic studies. To address these challenges, this paper implements an adaptive, multi-parameter model-free framework for predicting and compensating delays in co-simulated systems. The proposed approach combines an improved interface algorithm, the Damped Impedance Method (DIM), with an adaptive parameter-tuning predictor system to achieve accurate delay compensation without relying on complex signal transformations.

This framework enables efficient and stable dynamic analyses for geographically distributed power system models, overcoming limitations of traditional approaches while maintaining computational efficiency.

## II. Interface Algorithm

The established interface methods used in monolithic Power Hardware-in-the-Loop setups can be adapted for virtual coupling and integration of distributed or geographically dispersed real-time co-simulation experiments. The literature presents various co-simulation IAs, including the ITM and Partial Circuit Duplication (PCD) [1], [8], [37]. An accurate IA should enhance co-simulation accuracy and stability while facilitating interaction between subsystems in separate environments [7]. Desirable characteristics include low computational cost, robustness, flexibility, scalability, and high accuracy. Selecting the most suitable I A is crucial to ensure accuracy, stability, and efficiency, as different IAs offer varying suitability depending on subsystem characteristics and simulation environment. Therefore, careful evaluation of available IAs is essential for making an informed choice.

The ITM is a widely used co-simulation interface algorithm (IA) for integrating distinct subsystems within a co-simulation environment. It utilizes controlled voltage and current sources to emulate the behavior of remote subsystems on local ones [38]. However, its reliance on the assumption of zero transmission delay leads to degraded stability and accuracy under communication delays, rendering it unsuitable for real-time co-simulation environments where latency is critical. The ITM's transfer function is shown in (1), and its operational range, where Nyquist stability criteria are violated, is detailed in [38]. To overcome these limitations, alternative IAs such as the DIM have been developed. DIM introduces a damping impedance $Z^*$ between current and voltage sources, optimizing the convergence factor to improve precision and stability compared to the PCD algorithm, whose transfer function is shown in (2). DIM serves as a hybrid of PCD and ITM, where $Z^* \to \infty$ replicates ITM behavior, and $Z^* \to 0$ replicates PCD behavior, as illustrated in (3).

$$G_0 = \frac{Z_1(s)}{Z_2(s)} e^{-s\Delta t} \tag{1}$$

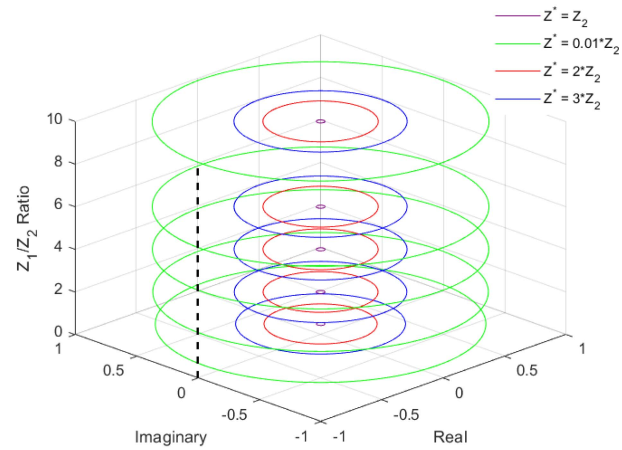


Fig. 1. Nyquist plot representing the operational range of the DIM system.

$$G_0 = \frac{Z_1(s)Z_2(s)}{[Z_1(s)+Z_{12}(s)][Z_2(s)+Z_{12}(s)]} e^{-s\Delta t} \tag{2}$$

$$G_0 = \frac{Z_1(s)[Z_2(s)-Z^*(s)]}{[Z_1(s)+Z_{12}(s)][Z_2(s)+Z_{12}(s)+Z^*(s)]} e^{-s\Delta t} \tag{3}$$

Fig. 1 shows the Nyquist plot for the DIM system. It indicates that when the coupling impedance ($Z^*$) matches the characteristic impedance, no gain in stability conditions occurs. Significant instability arises when $Z^*$ deviates from subsystem 1's impedance. Fig. 1 also confirms that DIM transitions between PCD and ITM behaviors based on $Z^*$ selection, with stability critically dependent on accurate $Z^*$ estimation. Absolute stability is ensured when $Z^*$ matches subsystem 2's impedance, making DIM superior in stability and computational efficiency compared to ITM and PCD [1], [37]. The DIM interface connects subsystems using specific arrangements of current and voltage sources. Two voltage sources are controlled by the voltage outputs of remote subsystems [1], while the current source in subsystem 1 is regulated by the current output from local subsystem 2. A damping impedance ($Z^*$) is placed between the current and voltage sources within subsystem 1 [37].

The proposed delay prediction and compensation method, discussed in the subsequent section, is designed to address the challenges associated with the typical interface signals of DIM like other IAs without relying on signal transformation. Unlike PHIL setups, DIM and other interface algorithms in GDRTCS environments do not utilize instantaneous current and voltage waveforms. This is because the shared network for communication introduces time-varying delays, packet loss, and reordering, which degrade waveform fidelity and introduce undesirable dynamics. To overcome these issues, rather than transforming waveforms into quantities that vary more slowly with respect to time, this work utilizes these time varying signals directly with their respective derivative with respect to time to make accurate prediction of the undelayed and undistorted coupling signal sent from the remote system, ensuring stability and accuracy in co-simulation environments despite the inherent communication delays.

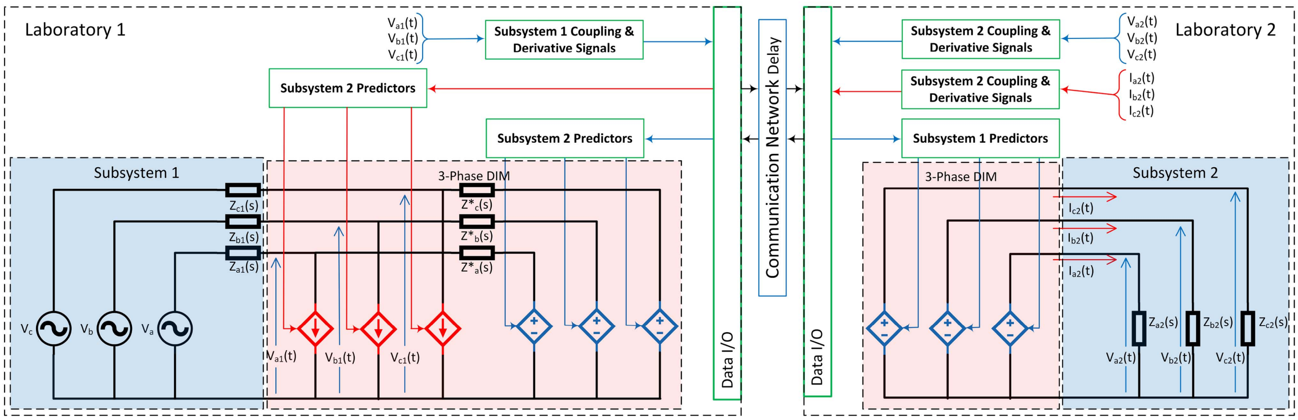


Fig. 2. Three-phase Damping Impedance Method with Implemented Predictors in the Two Laboratories.

## III. Interface Signal Delay Compensation

Within the DIM interface configuration in Fig. 2, three predictors model the closed-loop coupling variables and predict complex power system signals. In Subsystem 1 (Simulator 1, Laboratory 1), two predictors estimate undelayed coupling signals ($v_2(t)$ and $i_2(t)$) from Subsystem 2 (Simulator 2, Laboratory 2) [1], feeding control signals to voltage and current sources. A predictor in Subsystem 2 estimates the undelayed coupling signal ($v_1(t)$) from Subsystem 1 [37]. The interface employs a sliding mode control-based predictor [17], [39], which simplifies control to first-order behavior. It defines a sliding surface in the state space, ensuring robustness against disturbances, parameter uncertainties, and unmodeled dynamics, while achieving fast convergence. However, high control gains cause chattering, detrimental to precision, whereas low gains hinder convergence. Proper gain selection ensures convergence without oscillations.

Consider a single-input system with a non-linear structure described by (4), where $x(t)^n$ and $u(t)$ represent the system's output and input. The state vector is $x(t)$, with $f(x(t))$ and $g(x(t))$ capturing the non-linear dynamics. Although $f(x(t))$ is unknown, its uncertainty is bounded by a known continuous function of $x(t)$. Similarly, the control gain $g(x(t))$ has a known sign and is constrained by identifiable, continuous functions of $x(t)$. (4) models the system's behavior, providing insight into its dynamics. (4) represents the state-space model of the system, where $\dot{x}(t)$ captures state variables for calculating coupling signals at the virtual interface, and $u(t)$ denotes system inputs. The non-linear functions $f(x(t))$ and $g(x(t))$ govern state dynamics and interactions. While non-linearity complicates analysis and prediction, it is essential for modeling systems with complex dynamics [17]. Using mathematical models and analysis techniques provides insights into such systems' behavior. Tools like sliding mode control manage system inputs and outputs to meet performance specifications [39], which is crucial in applications across robotics, aerospace engineering, and power systems.

$$\dot{x}(t) = f(x(t)) + g(x(t)) \cdot u(t) \tag{4}$$

Sliding mode control provides a framework for analyzing the system in (4), ensuring optimal operation and adherence to performance specifications [39]. (5) define sliding surfaces within the two-dimensional phase plane, corresponding to the error systems $e_{v1}(t), e_{v2}(t)$, and $e_{i2}(t)$. These error systems represent control deviations for the coupling signal voltages $v_1(t)$ (from Simulator 1 to Simulator 2) and $v_2(t)$ (from Simulator 2 to Simulator 1), and current $i_2(t)$ (from Simulator 2 to Simulator 1). where: $\boldsymbol{I}$ is the $3 \times 3$ identity matrix, and $\alpha$, $\beta$, and $\gamma$ are the prediction system parameters.

$$\left(\alpha\mathbf{I} + \beta\frac{d}{dt}\mathbf{I} + \gamma\frac{d^2}{dt^2}\mathbf{I}\right)\begin{bmatrix} e_{v1}(t) \\ e_{v2}(t) \\ e_{i2}(t) \end{bmatrix} = \begin{bmatrix} 0 \\ 0 \\ 0 \end{bmatrix} \tag{5}$$

Within the error systems, parameter $\alpha$ dictates the surface's slope, which can be further adjusted with an additional term, introducing parameter $\beta$ and $\gamma$for greater flexibility. This approach uses a local model of the remote system to establish a model-based observer, with a sliding mode controller ensuring close convergence between the model's states and those of the remote system [17]. Thus, this design constructs a predictor's dynamic equation using a sliding surface, independent of a predefined remote system model. The goal is to develop a predictor that accurately tracks the remote system's actual state, avoiding the constraints of model-based approaches. State tracking errors between the predictor states ($\hat{v}_1(t)$, $\hat{v}_2(t)$, and $\hat{i}_2(t)$) and the initially transmitted remote system states ($v_1(t), v_2(t)$, and $i_2(t)$) are presented in (6).

$$\begin{bmatrix} e_{v1}(t) \\ e_{i2}(t) \\ e_{v2}(t) \end{bmatrix} = \begin{bmatrix} v_1(t) \\ i_2(t) \\ v_2(t) \end{bmatrix} - \begin{bmatrix} \hat{v}_1(t) \\ \hat{i}_2(t) \\ \hat{v}_2(t) \end{bmatrix} \tag{6}$$

In the absence of communication delays, (7) can be employed to derive the observer state's dynamic equation, ensuring the error system remains on the sliding surface. The principal objective of these observers is to predict the instantaneous response of subsystem 2 to the influence exerted by subsystem 1 and vice versa, neglecting any communication latency.

$$\begin{bmatrix} \frac{de_{v1}(t)}{dt} \\ \frac{de_{v2}(t)}{dt} \\ \frac{de_{i2}(t)}{dt} \end{bmatrix} = \begin{bmatrix} \frac{dv_1(t)}{dt} \\ \frac{dv_2(t)}{dt} \\ \frac{di_2(t)}{dt} \end{bmatrix} + \alpha \begin{bmatrix} v_1(t) - \hat{v}_1(t) \\ v_2(t) - \hat{v}_2(t) \\ i_2(t) - \hat{i}_2(t) \end{bmatrix} + \beta \begin{bmatrix} \frac{d}{dt}\left(v_1(t) - \hat{v}_1(t)\right) \\ \frac{d}{dt}\left(v_2(t) - \hat{v}_2(t)\right) \\ \frac{d}{dt}\left(i_2(t) - \hat{i}_2(t)\right) \end{bmatrix} + \gamma \begin{bmatrix} \frac{d^2}{dt^2}\left(v_1(t) - \hat{v}_1(t)\right) \\ \frac{d^2}{dt^2}\left(v_2(t) - \hat{v}_2(t)\right) \\ \frac{d^2}{dt^2}\left(i_2(t) - \hat{i}_2(t)\right) \end{bmatrix}. \tag{7}$$

However, practical applications encounter delays in receiving the remote signals ($v_1(t)$, $i_2(t)$, $v_2(t)$) and their derivatives ($\frac{d[v_1(t)]}{dt}$, $\frac{d[i_2(t)]}{dt}$, $\frac{d[v_2(t)]}{dt}$). Consequently, (7) is transformed into (8), incorporating the remote signals with their respective delays. It is important to note that $v_1(t)$ is transmitted from Subsystem 1 to Subsystem 2, while $i_2(t)$ and $v_2(t)$ are sent from Subsystem 2 to Subsystem 1.

$$\begin{bmatrix} \frac{de_{v1}(t)}{dt} \\ \frac{de_{v2}(t)}{dt} \\ \frac{de_{i2}(t)}{dt} \end{bmatrix} = \begin{bmatrix} \frac{dv_1(t-\tau)}{dt} \\ \frac{dv_2(t-\tau)}{dt} \\ \frac{di_2(t-\tau)}{dt} \end{bmatrix} + \alpha \begin{bmatrix} v_1(t-\tau) - \hat{v}_1(t) \\ v_2(t-\tau) - \hat{v}_2(t) \\ i_2(t-\tau) - \hat{i}_2(t) \end{bmatrix} + \beta \begin{bmatrix} \frac{d}{dt}\left(v_1(t-\tau) - \hat{v}_1(t)\right) \\ \frac{d}{dt}\left(v_2(t-\tau) - \hat{v}_2(t)\right) \\ \frac{d}{dt}\left(i_2(t-\tau) - \hat{i}_2(t)\right) \end{bmatrix} + \gamma \begin{bmatrix} \frac{d^2}{dt^2}\left(v_1(t-\tau) - \hat{v}_1(t)\right) \\ \frac{d^2}{dt^2}\left(v_2(t-\tau) - \hat{v}_2(t)\right) \\ \frac{d^2}{dt^2}\left(i_2(t-\tau) - \hat{i}_2(t)\right) \end{bmatrix} \tag{8}$$

Equation (8) incorporates the delayed remote states $v_1(t-\tau)$, $v_2(t-\tau)$, and $i_2(t-\tau)$, along with their derivatives. However, the difference terms on the right-hand side represent the discrepancy between the delayed states and the predicted states ($\hat{v}_1(t)$, $\hat{v}_2(t)$, $\hat{i}_2(t)$), not the actual state errors. This distinction is crucial because the predictor would track the delayed states rather than the current states ($v_1(t)$, $v_2(t)$, $i_2(t)$), making the prediction ineffective. Additionally, comparing states from different time instances (delayed vs. predicted) makes the term "state errors" inappropriate. A revised approach is needed to define a more meaningful error metric. Thus, (8) must be modified to account for delays in the predicted states. This leads to the new predictor designs in (9). The introduced delays in the predictor states ensure alignment with the actual remote system states, enabling accurate tracking.

$$\begin{bmatrix} \frac{de_{v1}(t)}{dt} \\ \frac{de_{v2}(t)}{dt} \\ \frac{de_{i2}(t)}{dt} \end{bmatrix} = \begin{bmatrix} \frac{dv_1(t-\tau)}{dt} \\ \frac{dv_2(t-\tau)}{dt} \\ \frac{di_2(t-\tau)}{dt} \end{bmatrix} + \alpha \begin{bmatrix} v_1(t-\tau) - \hat{v}_1(t-\tau) \\ v_2(t-\tau) - \hat{v}_2(t-\tau) \\ i_2(t-\tau) - \hat{i}_2(t-\tau) \end{bmatrix} + \beta \begin{bmatrix} \frac{d}{dt}\left(v_1(t-\tau) - \hat{v}_1(t-\tau)\right) \\ \frac{d}{dt}\left(v_2(t-\tau) - \hat{v}_2(t-\tau)\right) \\ \frac{d}{dt}\left(i_2(t-\tau) - \hat{i}_2(t-\tau)\right) \end{bmatrix} + \gamma \begin{bmatrix} \frac{d^2}{dt^2}\left(v_1(t-\tau) - \hat{v}_1(t-\tau)\right) \\ \frac{d^2}{dt^2}\left(v_2(t-\tau) - \hat{v}_2(t-\tau)\right) \\ \frac{d^2}{dt^2}\left(i_2(t-\tau) - \hat{i}_2(t-\tau)\right) \end{bmatrix} \tag{9}$$

The observer's output functions in (9) estimate the non-delayed states ($\hat{v}_1(t)$, $\hat{i}_2(t)$, and $\hat{v}_2(t)$) of the remote subsystem. Modifying these equations to incorporate delays results in a first-order time-delay observer parameterized by $\alpha$, $\beta$, and $\gamma$. When $\gamma$ and $\beta$ are zero, the predictor becomes a single-parameter system with reduced design freedom. Assuming all terms on the right-hand side of (9) are known exactly, the designed predictors aim to minimize the discrepancy between their predicted states and the actual remote system states. Notably, the predictor design requires no knowledge of the underlying system dynamics. The expressions for the predicted signals are presented in (10).These expressions incorporate error feedback loops within the predictors, effectively compensating for propagated errors. They are derived by integrating the final dynamic equation, as shown in (8) for respective coupling signals in different subsystems.

$$\begin{bmatrix} \hat{v}_1(t) \\ \hat{v}_2(t) \\ \hat{i}_2(t) \end{bmatrix} = \begin{bmatrix} v_1(t-\tau) \\ v_2(t-\tau) \\ i_2(t-\tau) \end{bmatrix} + \frac{\alpha}{1+\beta+\gamma} \int \begin{bmatrix} v_1(t-\tau) - \hat{v}_1(t-\tau) \\ v_2(t-\tau) - \hat{v}_2(t-\tau) \\ i_2(t-\tau) - \hat{i}_2(t-\tau) \end{bmatrix} dt + \frac{\beta}{1+\gamma} \begin{bmatrix} v_1(t-\tau) - \hat{v}_1(t-\tau) \\ v_2(t-\tau) - \hat{v}_2(t-\tau) \\ i_2(t-\tau) - \hat{i}_2(t-\tau) \end{bmatrix} + \gamma \frac{d}{dt} \begin{bmatrix} v_1(t-\tau) - \hat{v}_1(t-\tau) \\ v_2(t-\tau) - \hat{v}_2(t-\tau) \\ i_2(t-\tau) - \hat{i}_2(t-\tau) \end{bmatrix}. \tag{10}$$

The delay ($\tau$) can be determined by synchronizing clocks at both ends of the communication channel and using timestamps on data packets. The observer functions as a second-order time-delay system, with $\alpha$, $\beta$ and $\gamma$ as the design parameters for predicting the state variables at the current time ($t$). Using (11), the transfer function (the ratio of the error signal to the coupling error) can be derived for both single-parameter and multi-parameter predictor systems. The two parameters will influence system performance differently; thus, using all of $\alpha$, $\beta$ and $\gamma$ as tuning parameters significantly expands the design space, offering the potential for superior system performance.

$$\frac{E(s)}{C(s)} = \frac{s}{s + \gamma s^2 e^{-\tau s} + \beta s e^{-\tau s} + \alpha e^{-\tau s}} \tag{11}$$

This shows the transfer function a multi-parameter system and the characteristic equation is given by (12):

$$s + \gamma s^2 e^{-\tau s} + \beta s e^{-\tau s} + \alpha e^{-\tau s} = 0 \tag{12}$$

To analyze the multi-parameter (12), the exponential terms are eliminated by multiplying the entire equation by $e^{\tau s}$ as given in (13):

$$s e^{\tau s} + \gamma s^2 + \beta s + \alpha = 0 \tag{13}$$

This simplifies the equation by isolating the terms involving $s$ and the time delay $\tau$. For stability analysis, substitute $s = j\omega$, where $\omega$ is the frequency of oscillation. This transforms (13) into (14):

$$j\omega e^{j\omega\tau} + \gamma (j\omega)^2 + \beta j\omega + \alpha = 0 \tag{14}$$

Using Euler's formula, expand $e^{j\omega\tau}$ into its trigonometric components: $e^{j\omega\tau} = \cos(\omega\tau) + j\sin(\omega\tau)$ . Substituting this back into (14) gives (15):

$$j\omega(\cos(\omega\tau) + j\sin(\omega\tau)) + \gamma(-\omega^2) + \beta j\omega + \alpha = 0 \tag{15}$$

Separating into real and imaginary parts, $j\omega$ is distributed on the left-hand side as $j\omega\cos(\omega\tau) - \omega\sin(\omega\tau) + \gamma(-\omega^2) + \beta j\omega + \alpha = 0$ and this is grouped as (16) and (17), respectively:

$$-\omega\sin(\omega\tau) - \gamma\omega^2 + \alpha = 0 \tag{16}$$

$$\omega\cos(\omega\tau) + \beta\omega = 0 \tag{17}$$

Consequently, solving for $\alpha$, $\beta$, and $\gamma$ from the real and imaginary parts, the expressions for $\alpha$, $\beta$, and $\gamma$ are given as (18) and (19):

$$\alpha = \omega\sin(\omega\tau) + \gamma\omega^2 \tag{18}$$

$$\beta = -\cos(\omega\tau) \tag{19}$$

The frequency $\omega$ is expressed in terms of $\beta$ from the imaginary part as $\cos(\omega\tau) = -\beta$ and solving for $\omega\tau$ is given as $\omega\tau = \arccos(-\beta)$. Thus,the frequency is expressed as (20)

$$\omega = \frac{1}{\tau}\arccos(-\beta) \tag{20}$$

Substituting (20) into (18) will give (21). Simplifying $\sin(\arccos(x))$ using the trigonometric identity $\sin(\arccos(x)) = \sqrt{1-x^2}$ and substituting this identity gives (22):

$$\alpha = \frac{1}{\tau}\arccos(-\beta)\sin\left(\arccos(-\beta)\right) + \gamma\left(\frac{1}{\tau^2}(\arccos(-\beta))^2\right) \tag{21}$$

$$\alpha = \frac{1}{\tau}\arccos(-\beta)\sqrt{1-\beta^2} + \frac{\gamma}{\tau^2}(\arccos(-\beta))^2 \tag{22}$$

Consequently, this is the stability boundary for $\alpha$ in terms of $\beta$, $\gamma$, and $\tau$ and forms the open-loop stability boundary for the multi-parameter system. The relationship between $\alpha$, $\beta$, and $\gamma$ is further analyzed to determine specific stability regions as shown in Fig. 3.

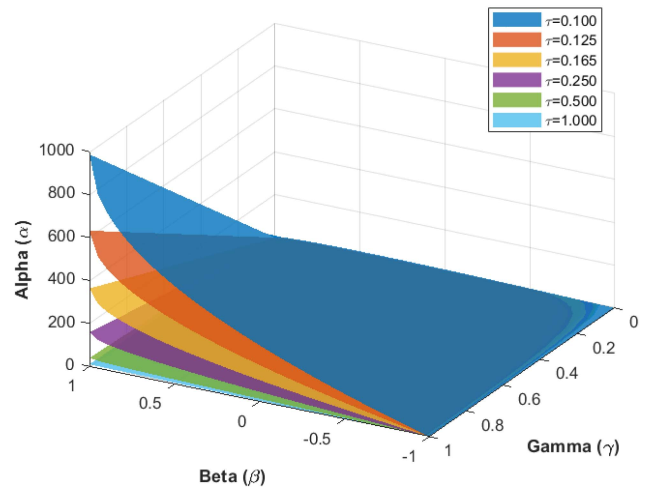


Fig. 3. Stability boundaries of the tuning parameters $\alpha$, $\beta$, $\gamma$ as a function of delay $\tau$ for a multi-parameter predictor system.

The stability limits for the three design parameters $\alpha$, $\beta$, and $\gamma$ are derived by considering the system dynamics under various delays $\tau$. As shown in Fig. 3, the stability boundaries contract with increasing $\tau$, indicating reduced design flexibility. However, the inclusion of the third parameter $\gamma$ extends the permissible values of $\alpha$ and $\beta$ by providing an additional degree of freedom in the design space. This compensatory effect mitigates the destabilizing influence of larger delays, enabling greater stability flexibility compared to single-parameter systems. For moderate values of $\gamma$, the stability region expands significantly, even under higher delays, underscoring its critical role in enhancing the predictor system's robustness.

The transfer function for the multi-parameter system is given as (11) and replacing $s$ with $j\omega$ to analyze in the frequency domain gives (23):

$$\frac{E(j\omega)}{C(j\omega)} = \frac{j\omega}{j\omega + \gamma(j\omega)^2 e^{-j\omega\tau} + \beta j\omega e^{-j\omega\tau} + \alpha e^{-j\omega\tau}} \tag{23}$$

The denominator in (23) is separated into its real and imaginary components and the frequency domain magnitude is derived as given in (24). The frequency response $M(\omega)$ is the ratio of the numerator (state-tracking error) magnitude to the denominator (coupling error).

$$M(\omega) = \frac{|\omega|}{\sqrt{\begin{aligned}&\left(\gamma\omega^2\cos(\omega\tau) + \beta\omega\cos(\omega\tau) + \alpha\cos(\omega\tau)\right)^2\\ &+\left(\omega - \gamma\omega^2\sin(\omega\tau) - \beta\omega\sin(\omega\tau) - \alpha\sin(\omega\tau)\right)^2\end{aligned}}} \tag{24}$$

System stability, while necessary, is not sufficient for effective delay compensation, as a stable observer might not reduce prediction error below the coupling error. Frequency domain analysis assesses the observer's delay compensation effectiveness. The stability margin for the $\alpha$ parameter in a single-parameter predictor system ranges from 0 to $\frac{\pi}{2\tau}$ [39]. In this study, the

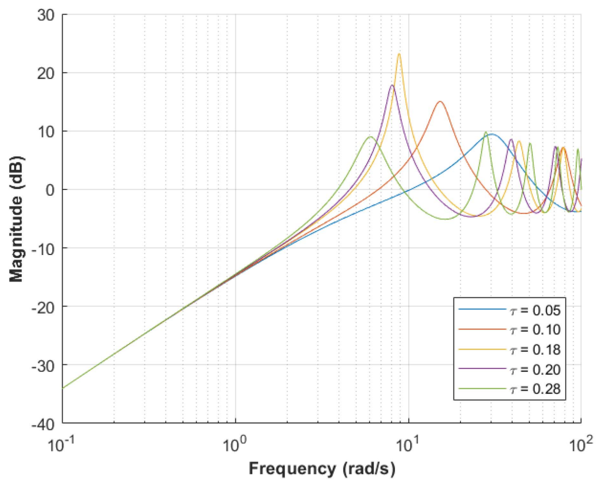


Fig. 4. Impact of varying delay values $\tau$ on a multi-parameter prediction system with fixed $\alpha$, $\beta$, and $\gamma$.

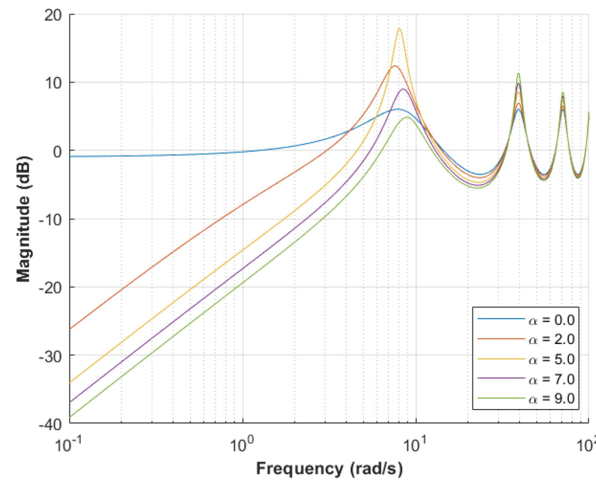


Fig. 5. Impact of parameter $\alpha$ on the predictor's frequency response with fixed $\beta$, $\gamma$ and $\tau$.

values of $\alpha$ were set to 0.95 and 0.85 of the maximum allowable limit for the single- and multi-parameter predictor systems, respectively, in order to avoid operating exactly at the stability boundary. The lower $\alpha$ value used in the multi-parameter system reflects the increased flexibility afforded by introducing additional tuning parameters $\beta$ and $\gamma$, which allows the system to remain stable without pushing $\alpha$ to its critical threshold. Multi-parameter predictors offer greater tuning flexibility. Fig. 4 further analyzes varying delay values ($\tau$) with fixed $\alpha$, $\beta$ and $\gamma$ for the prediction system. This shows that increasing $\tau$ raises the high-frequency error gain, medium-frequency overshoot, and reduces bandwidth. However, the low-frequency error gain and high-frequency oscillation amplitude remain independent of $\tau$. To mitigate oscillations and enhance $\beta$ and $\gamma$ flexibility in the multi-parameter system, $\alpha$ is reduced.

The stability limitations of the multi-parameter predictor are similar to those of a single-parameter predictor as delay ($\tau$) increases, with the stable operating region shrinking and reducing the range of design choices that ensure stability as given in Fig. 3. Single and multi predictor designs face the challenge of compensating for larger delays. However, the additional $\beta$ and $\gamma$ parameters in the multi-parameter predictor offer an advantage by allowing a larger maximum allowable delay for stability.

Figs. 5, 6 and 7 analyze the effectiveness of delay compensation in the multi-parameter predictor in the frequency domain. Fig. 5 shows the effect of $\alpha$ (with fixed $\beta$, $\gamma$ and $\tau$). Increasing $\alpha$ reduces low-frequency error gain but initially decreases bandwidth before a gradual rise, also increasing overshoot in medium frequencies. Fig. 6 shows the impact of parameter $\beta$ (with fixed $\alpha$, $\gamma$ and $\tau$). While $\beta$ doesn't affect low-frequency error gain, it reduces bandwidth and increases overshoot at higher frequencies, especially for negative $\beta$. This suggests restricting $\beta$ to [0, 1] for practical use. Positive $\beta$ can improve bandwidth and overshoot, beneficial for low-bandwidth systems. Fig. 7 shows that the addition of a smaller $\gamma$ helps maintain stability by keeping the magnitude response relatively flat across

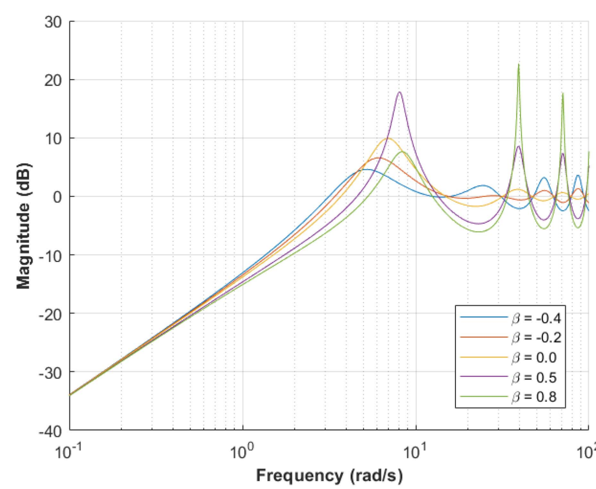


Fig. 6. Impact of parameter $\beta$ on the predictor's frequency response with fixed $\alpha$, $\gamma$ and $\tau$.

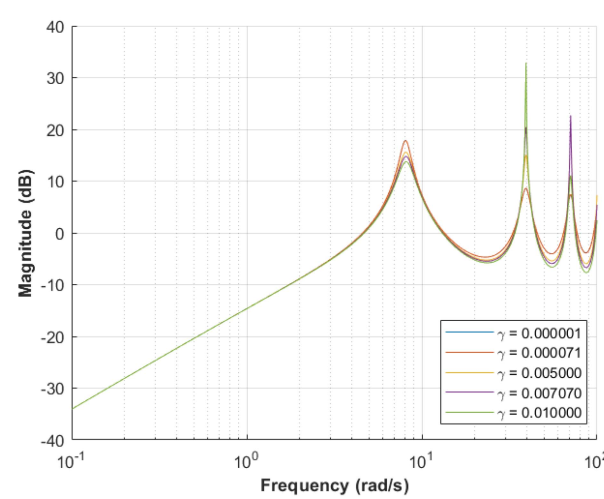


Fig. 7. Impact of parameter $\gamma$ on the predictor's frequency response with fixed $\alpha$, $\gamma$ and $\tau$.

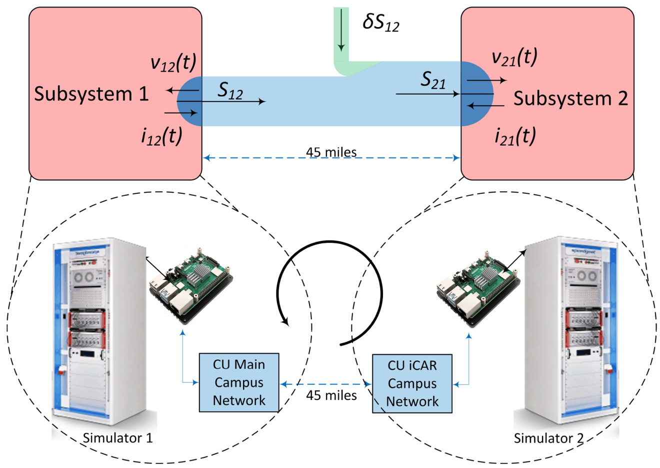


Fig. 8. Two virtually coupled subsystems 1 and 2 exchanging power through a power bond $1-2$ as $S_{12}=v_{12}\cdot i_{12}$.

a broader frequency range. At higher frequencies, the differences in the magnitude response due to $\gamma$ become more noticeable. For larger $\gamma$ values, the system exhibits increased gain at high frequencies compared to smaller $\gamma$. The parameter $\alpha$, $\beta$, and $\gamma$ does have different frequency responses on the system and these contrasting effects of $\alpha$, $\beta$ and $\gamma$ highlight the advantage of using a multi parameter system for design flexibility.

The flow and conservation of energy between virtually coupled real-time digital simulators and laboratory assets can be effectively analyzed using power bonds, which establish direct energetic links between subsystems [40]. Power bonds are defined by two variables—flow (e.g., current, velocity) and effort (e.g., voltage, force)—whose product represents physical power. For example, in electrical systems, the interface current ($i_{12}$) and voltage ($v_{12}$) define the power bond, with power given by $S_{12}=v_{12}\cdot i_{12}$, representing the rate of energy exchange. In co-simulation, subsystems progress independently in time, and communication delays introduce coupling errors, leading to energy residuals that distort system dynamics and compromise the accuracy, stability, and reliability of the coupled system. Monitoring voltage and current at power ports enables the analysis of energy flow and conservation, forming the basis of bond graph theory and ensuring energy consistency in the coupled system.

The residual power is the power discrepancy introduced during the time step, which results from the mismatch between the power transmitted between the subsystems as shown in Fig. 8. In a power system co-simulation environment, each subsystem operates independently. Thus, Subsystem 1 calculates its voltage $v_{12}(t)$ and current $i_{12}(t)$ while Subsystem 2 computes $v_{21}(t)$ and $i_{21}(t)$ at different time instance with the presence of communication delay. If there is a delay the coupling variable $v_{12}(t)\neq v_{21}(t)$ and $i_{12}(t)\neq i_{21}(t)$. Thus, due to this asynchronous exchange of coupling signals, energy conservation will be violated as the power exchanged between the subsystems is not consistent. Therefore:

$$v_{12}(t)\cdot i_{12}(t)\neq v_{21}(t)\cdot i_{21}(t) \tag{25}$$

The coupling variables will, therefore, be computed by the subsystems at different time steps. The delayed signals for $v_{12}(t)$, $i_{12}(t)$, $v_{21}(t)$, and $i_{21}(t)$ introduce errors into the power transfer, leading to an imbalance in the power exchange. From (25), the power conservation violation can be expressed as:

$$S_{12}\neq S_{21} \tag{26}$$

This indicates discrepancies in the total power exchange between the subsystems, leading to a power imbalance. Thus, the residual power arises due to the discrepancy between the power exchanged by the two subsystems during the co-simulation. This residual power is caused by the independent time integration of the two simulators as a result of the communication delay. When the voltage and current in one subsystem are updated at different times from the other subsystem, the coupling signals transferred are not accurately accounted for. This incorrect power generation or loss is expressed as Residual power $\delta S_{12}$ in (27) which affects the overall accuracy and stability of the co-simulation. Thereby distorting the overall system dynamics.

$$\delta S=|S_{12}-S_{21}| \tag{27}$$

Consequently, the measurement of discrepancies in power at the coupling interfaces, or residual power, is a critical performance metric for evaluating the fidelity and accuracy of power co-simulation. This will indicate the extent to which power conservation violations are mitigated and residual power in the interface.

## IV. Experimental Results

This work describes the virtual integration of laboratory assets across Clemson University's main campus in Clemson, SC, and the Clemson University International Center for Automotive Research (iCAR) Greenville campus, SC, using VILLAS nodes. VILLAS nodes act as gateways for processing and forwarding data between real-time simulators, facilitating joint experiments with delay estimation. For a collaborative experiment, the system was partitioned into two subsystems located in separate laboratories on each campus. The basic hardware setups in Remote Laboratory 1 (housing Subsystem 1) and Remote Laboratory 2 (housing Subsystem 2) are depicted in Fig. 9. Synchronization of the Speedgoat Performance Real-Time Target Machine simulator (Simulators 1 and 2) to the GNSS SEL-2488 Satellite-Synchronized Network Clock via the IEEE 1588 PTP ensured precise alignment and synchronization of the entire system, enabling accurate alignment of experimental results and estimation of latency. The estimated communication delays between these laboratories, critical real-time inputs to the prediction system, are illustrated in Fig. 10. Analysis of the Nyquist plots for various interface algorithms further justifies the selection of DIM over ITM and PCD, ensuring system stability and simulation fidelity [1].

The test system used in this study is the IEEE 14-bus system, a benchmark for representing transmission and distribution networks in co-simulation studies. The system is partitioned at Bus 14, a load bus, to delineate the transition between the transmission and distribution networks. Bus 14 represents a

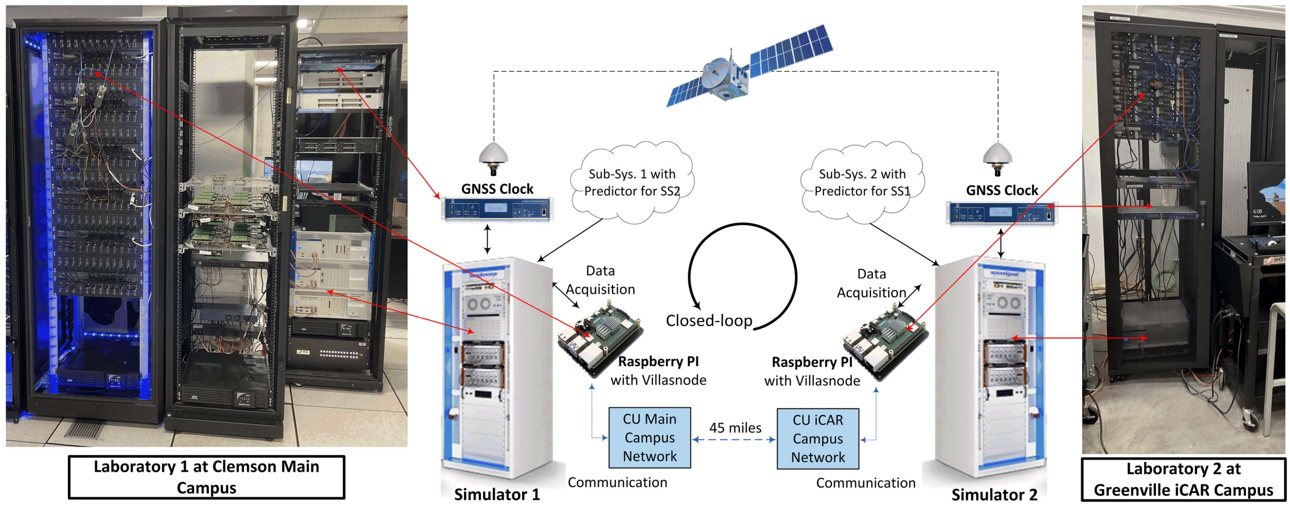


Fig. 9. Basic hardware setups in the Two laboratory facilities: Remote Laboratory 1 (housing Subsystem 1) and Remote Laboratory 2 (housing Subsystem 2).

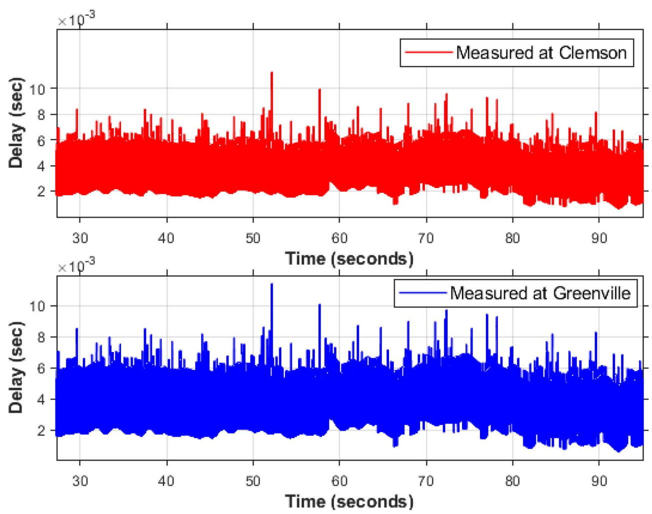


Fig. 10. Estimated communication delays between the two laboratories.

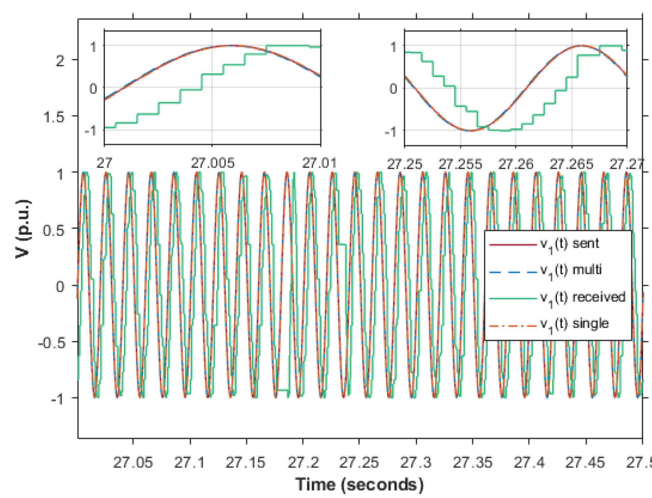


Fig. 11. Comparison between the transmitted voltage signal ($v_1(t)$) from Subsystem 1, the predicted signals ($\hat{v}_1(t)$) received and uncompensated signal received in Subsystem 2 for the single-parameter and multi-parameter prediction approaches.

typical distribution node characterized by a specified voltage of 1 p.u. under nominal operating conditions. The active and reactive power demands at this bus are 0.149 MW and 0.05 MVAR, respectively, reflecting realistic load conditions. This partitioning enables detailed co-simulation studies by separating the high-voltage transmission network from the medium-voltage distribution network, thereby allowing the examination of interactions between the two subsystems [41].

Figs. 11, 12, and 13 show the impact of communication delays on coupling signals ($v_1(t)$, $v_2(t)$, and $i_2(t)$) acting as control inputs for the controlled voltage source in Simulator 2 and the controlled voltage and current sources in Simulator 1. These figures show the discrepancy between the transmitted reference signal and the delayed received signal, necessitating a prediction algorithm to counteract the delay effects. The coupling signals exchanged between the simulators exhibit a latency shift between transmission and reception. In addition to the traditional DIM coupling signals ($v_1(t)$, $v_2(t)$, and $i_2(t)$), their time derivatives are also transmitted and received at the respective remote simulators, similarly impacted by latency.

To validate the theoretical analysis and gain insights into the transient behavior of the single- and multi-parameter predictors in a power system context, this work applied the predictors to the three coupling signals within the DIM model. This process involved using the observer's predictions for the control signals of the controlled voltage source in Simulator 2 ($v_1(t)$), the controlled voltage source in Simulator 1 ($v_2(t)$), and the controlled current source in Simulator 1 ($i_2(t)$), followed by an evaluation of their performance. The obtained results substantiate the theoretical basis and provide insights into the dynamics of the three predictors. The real-time experiment offers practical

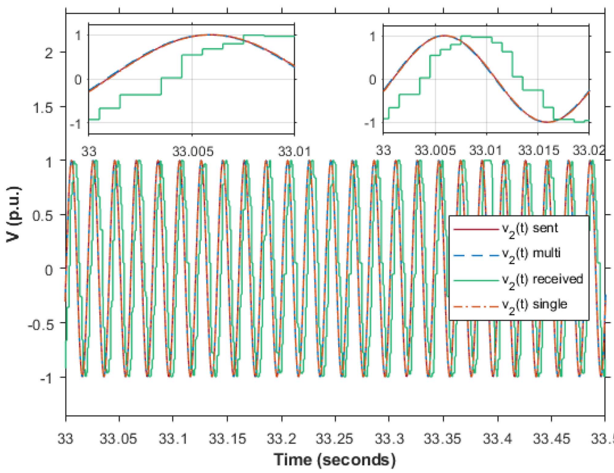


Fig. 12. Comparison between the transmitted voltage signal ($v_2(t)$) from Subsystem 2 and the predicted signals ($\hat{v}_2(t)$) received and uncompensated signal received in Subsystem 1 for the single-parameter and multi-parameter methods.

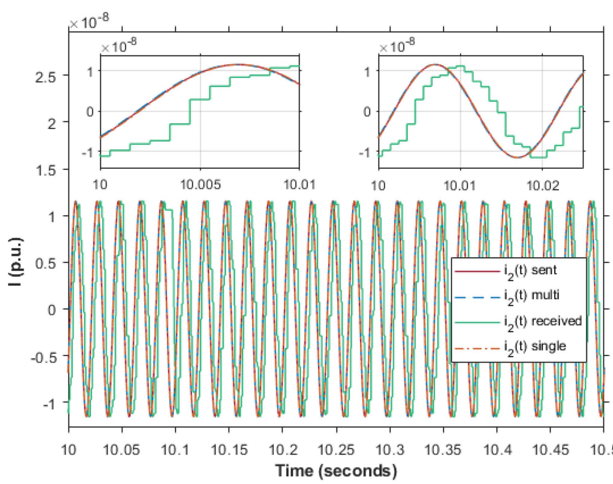


Fig. 13. Comparison of the transmitted current signal ($i_2(t)$) from Subsystem 2 and the predicted signals ($\hat{i}_2(t)$) received and uncompensated signal received in Subsystem 1 for the single-parameter and multi-parameter prediction approaches.

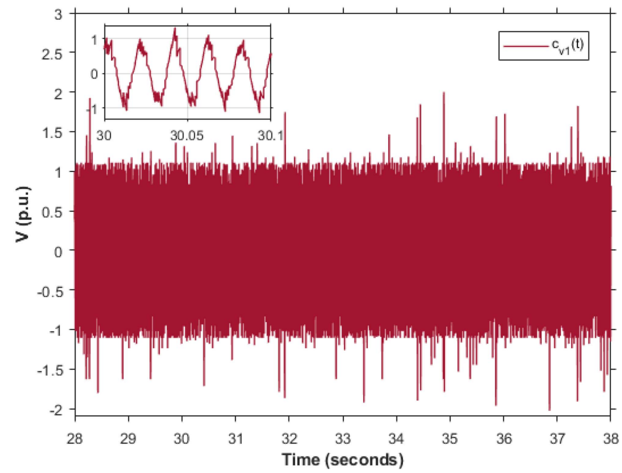


Fig. 14. Coupling error for the transmitted voltage prediction system using single-parameter and multi-parameter approaches for $v_1(t)$.

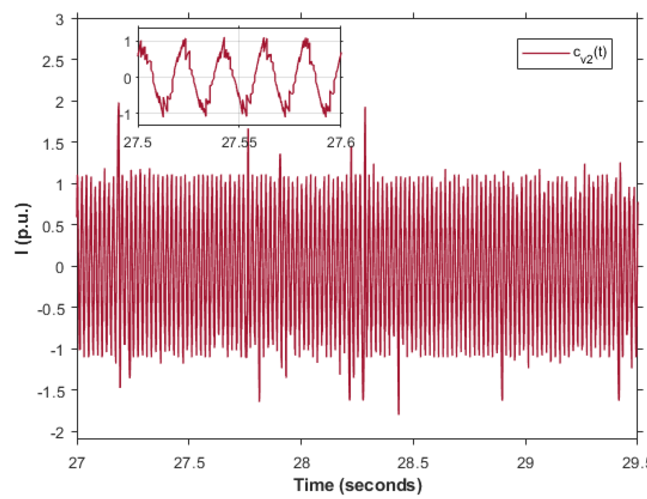


Fig. 15. Coupling error for the transmitted current prediction system using single-parameter and multi-parameter approaches for $v_2(t)$.

experience and reveals limitations or unforeseen issues not evident in theoretical analysis. At 60 Hz, variations in real-time delay can introduce amplitude shifts and distort the predicted signal, with severity proportional to the delay magnitude. An offline characterization quantifies the amplitude shift for different delay magnitudes, leading to a normalization factor look-up table. This table enables real-time adjustment of the predicted signal based on measured delay, mitigating the impact on prediction accuracy.

This work is crucial for developing robust prediction algorithms for real-time power system operations as Figs. 11, 12, and 13 show a relative alignment of the predicted signals with the undelayed transmitted signals. Fig. 11 compares the transmitted voltage signal ($v_1(t)$) from Subsystem 1 with the predicted signals ($\hat{v}_1(t)$) received in Subsystem 2 for the single- and multi-parameter approaches. Similarly, Fig. 12 compares the transmitted voltage signal ($v_2(t)$) from Subsystem 2 with the predicted signals ($\hat{v}_2(t)$) received in Subsystem 1. Finally, Fig. 13 compares the transmitted current signal ($i_2(t)$) from Subsystem 2 with the predicted signals ($\hat{i}_2(t)$) received in Subsystem 1. These comparisons demonstrate the predictors' ability to accurately forecast the original undelayed remote signal, even with only the delayed signals available.

Communication delay introduces a coupling error, defined as the difference between the transmitted (undelayed) and received (delayed) signals, which quantifies the impact of delay on the received signals. This error serves as the input to the prediction system, which aims to minimize it. State tracking error, on the other hand, represents the difference between the predicted signal and the original undelayed signal from the remote simulator, reflecting the prediction system's output performance. Fig. 14 shows the coupling error $c_{v1}(t)$ for $v_1(t)$, which is similar to error $c_{v2}(t)$ for $v_2(t)$ shown in Fig. 15 except for transients in

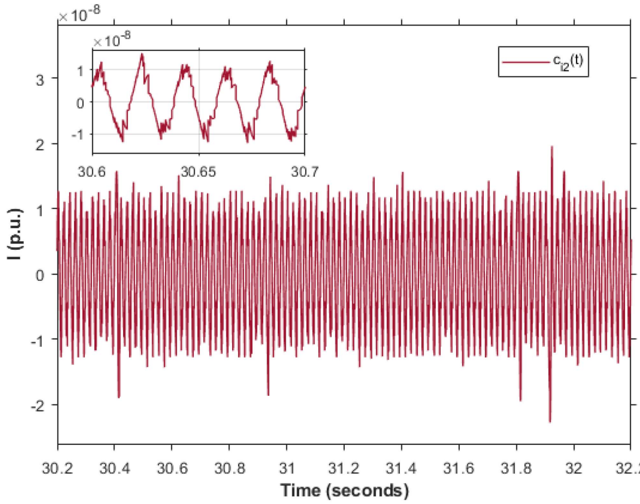


Fig. 16. Coupling error for the transmitted voltage prediction system using single-parameter and multi-parameter approaches for $i_2(t)$.

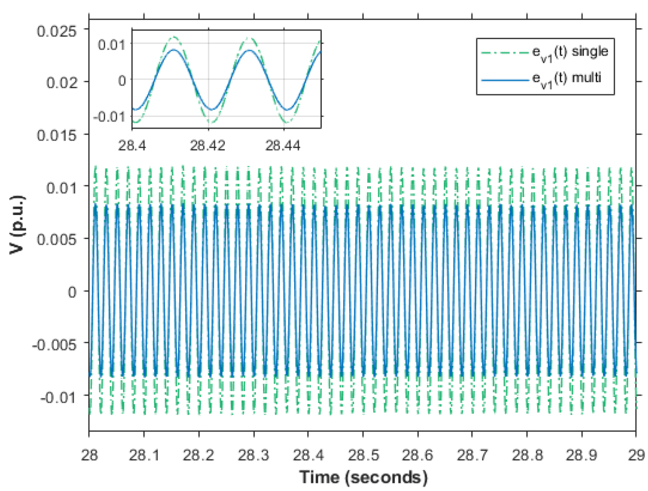


Fig. 17. State-tracking error for the transmitted voltage prediction system using single-parameter and multi-parameter approaches for $v_1(t)$.

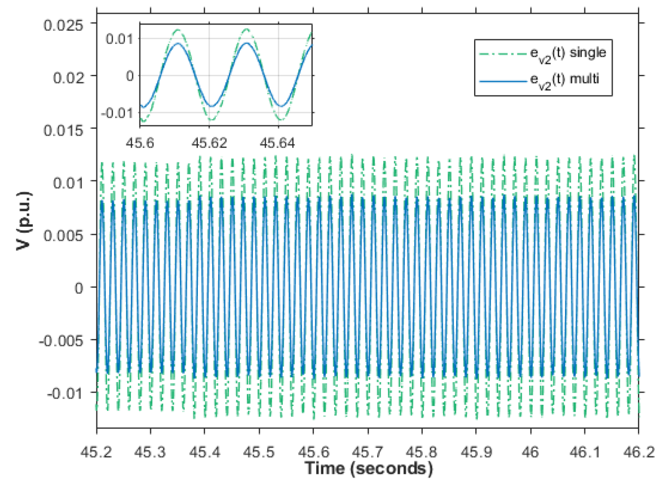


Fig. 18. State-tracking error for the transmitted voltage prediction system using single-parameter and multi-parameter approaches for $v_2(t)$.

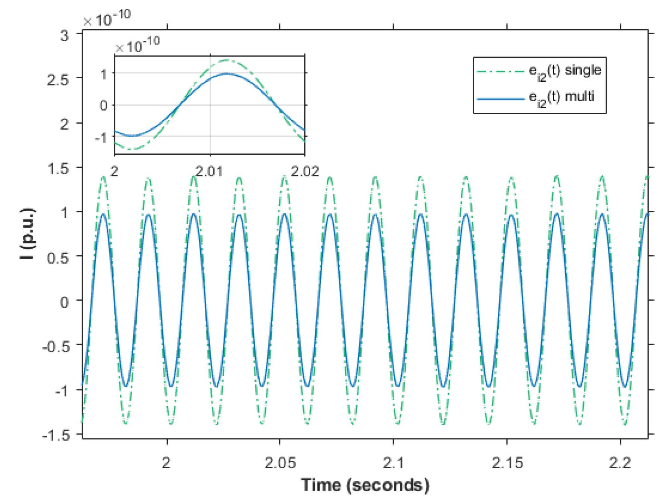


Fig. 19. State-tracking error for the transmitted voltage prediction system using single-parameter and multi-parameter approaches for $i_2(t)$.

$c_{v2}(t)$ due to differences in delay estimation and phase. Fig. 16 shows the coupling error$c_{i2}(t)$ for $i_2(t)$.

Fig. 17 illustrates state-tracking errors for the $v_1(t)$ prediction system using single- and multi-parameter approaches, while Figs. 18 and 19 show state-tracking errors for the $v_2(t)$ and $i_2(t)$ prediction systems, respectively.

By analyzing both coupling and state tracking errors, we can evaluate the effectiveness of our prediction system. For all three coupling signals in the DIM interface, the state tracking errors are significantly smaller than the coupling errors, highlighting the prediction system's effectiveness in mitigating communication delay. Table I compares these errors across different delay values. As seen, prediction errors remain significantly lower than coupling errors for the three coupling signals. The additional tuning parameters $\beta$ and $\gamma$ influence state-tracking errors. As shown in Figs. 17, 18, and 19, the predictors achieve minimized state-tracking error with the inclusion of $\beta$ and $\gamma$. In steady-state conditions, the ratio of state-tracking error magnitude to coupling error magnitude decreases, consistent with the stability analysis based on Bode plots. This reinforces the efficacy of the proposed predictors, particularly the multi-parameter version, in enhancing state-tracking performance. The multi-parameter predictor framework improves delay compensation capabilities while retaining its model-free nature, enhancing prediction accuracy across the three coupling signals used in power system co-simulation. Additionally, power balance preservation is critical for energy conservation, reflecting the fidelity of real-time co-simulation experiments.

The trends observed in Fig. 3 are supported by the $\alpha$ values used in simulations for different delay values, as shown in Table II. With increasing delay ($\tau$), the theoretical upper boundary for $\alpha$ reduces, limiting stability. The single-parameter predictor operates near this limit (approximately 95% of $\alpha_{\max}$), confirming that it lacks flexibility to accommodate additional

TABLE I
PEAK COUPLING VS PREDICTION ERRORS UNDER DIFFERENT DELAYS FOR SINGLE AND MULTI-PARAMETER SYSTEMS

| $\tau$ (s) | $c_{v1}$ | $e_{v1}-multi$ | $e_{v1}-single$ | $c_{v2}$ | $e_{v2}-multi$ | $e_{v2}-single$ | $c_{i2}$ | $e_{i2}-multi$ | $e_{i2}-single$ |
|---|---|---|---|---|---|---|---|---|---|
| 0.001 | 0.2826 | 0.005746 | 0.008292 | 0.2826 | 0.005746 | 0.008374 | 3.3370E-09 | 6.5390E-11 | 9.5680E-11 |
| 0.002 | 0.5652 | 0.005763 | 0.008301 | 0.5652 | 0.005763 | 0.008377 | 6.7080E-09 | 6.5560E-11 | 9.5700E-11 |
| 0.003 | 0.8378 | 0.005768 | 0.008311 | 0.8378 | 0.005768 | 0.008377 | 1.0000E-08 | 6.5790E-11 | 9.5730E-11 |
| 0.004 | 1.103 | 0.005771 | 0.008322 | 1.104 | 0.005771 | 0.008383 | 1.3400E-08 | 6.6070E-11 | 9.5770E-11 |
| 0.005 | 1.356 | 0.005844 | 0.008333 | 1.356 | 0.005844 | 0.008383 | 1.6550E-08 | 6.6210E-11 | 9.5780E-11 |
| 0.006 | 1.595 | 0.006586 | 0.008342 | 1.595 | 0.006586 | 0.008384 | 1.9530E-08 | 6.6620E-11 | 9.5780E-11 |
| 0.007 | 1.803 | 0.006795 | 0.008353 | 1.803 | 0.006795 | 0.008385 | 2.1750E-08 | 6.6760E-11 | 9.5780E-11 |
| 0.008 | 1.970 | 0.006819 | 0.008354 | 1.970 | 0.006819 | 0.008385 | 2.3530E-08 | 6.6090E-11 | 9.5790E-11 |
| 0.009 | 2.086 | 0.006832 | 0.008362 | 2.086 | 0.006832 | 0.008377 | 2.4610E-08 | 6.8340E-11 | 9.5800E-11 |
| 0.010 | 2.141 | 0.007386 | 0.008807 | 2.141 | 0.007386 | 0.008374 | 2.4910E-08 | 6.8480E-11 | 9.5810E-11 |

TABLE II
MAXIMUM ALLOWABLE AND MEASURED $\alpha$ VALUES FOR SINGLE- AND MULTI-PARAMETER PREDICTORS

| $\tau$ (s) | $\alpha_{Maximum}$ | $\alpha_{Multi}$ | $\alpha_{Single}$ |
|---|---|---|---|
| 0.001 | 1.5714E+03 | 1.2571E+03 | 1.4929E+03 |
| 0.002 | 7.8571E+02 | 6.2857E+02 | 7.4643E+02 |
| 0.003 | 5.2381E+02 | 4.1905E+02 | 4.9762E+02 |
| 0.004 | 3.9286E+02 | 3.1429E+02 | 3.7321E+02 |
| 0.005 | 3.1429E+02 | 2.5143E+02 | 2.9857E+02 |
| 0.006 | 2.6190E+02 | 2.0952E+02 | 2.4881E+02 |
| 0.007 | 2.2449E+02 | 1.7959E+02 | 2.1327E+02 |
| 0.008 | 1.9643E+02 | 1.5714E+02 | 1.8661E+02 |
| 0.009 | 1.7460E+02 | 1.3968E+02 | 1.6587E+02 |
| 0.010 | 1.5714E+02 | 1.2571E+02 | 1.4929E+02 |

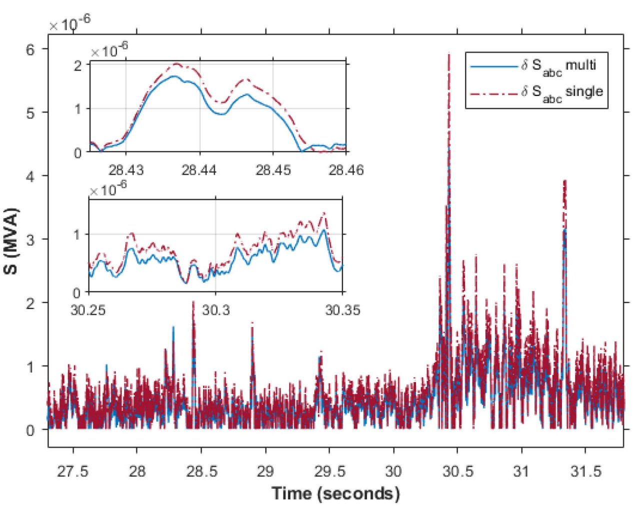


Fig. 20. Estimated Residual Powers and Interface Powers at the interface 1 and 2 under the two predictors.

tuning. In contrast, the multi-parameter predictor adopts a more conservative $\alpha$ (approximately 85% of $\alpha_{\max}$), thereby staying well within the stability region shown in Fig. 3 and enabling stable tuning of $\beta$ and $\gamma$. This empirical choice supports the theoretical relationship between $\alpha$, $\tau$, and the tuning space observed in Fig. 3.

In addition to analyzing coupling and prediction or state-tracking errors, the residual power between the two subsystems was evaluated to understand the impact of time delays on the proposed delay compensation technique across the three phases of the power subsystems. Fig. 20 shows the estimated residual complex power, which indicates the discrepancies in interface powers at interfaces 1 and 2 under the single and multi-parameter predictors. $\delta S_{abc}$-single and $\delta S_{abc}$ -multi represent three-phase residual complex power between the two interfaces for the single and multi predictors. This difference serves as a metric to evaluate real-time co-simulation accuracy. The power difference between interfaces 1 and 2 must approach zero to uphold power conservation.

## V. CONCLUSION

This paper proposes a model-free adaptive framework for predicting and compensating delays in power system co-simulation, eliminating the need for complex signal processing, improving parallel computation and enabling broader applicability. The framework, implemented on the three coupling signals of the damping impedance interface algorithm, includes both single- and multi-parameter model-free predictors. Nyquist plot analysis justifies the selection of the DIM, with stability analysis exploring the relationship between tuning parameters and predictor stability. Dynamic performance evaluations validate the design and theoretical analysis of both predictors. The multi-parameter predictor demonstrates superior delay compensation and expanded operational stability, making it more robust across various scenarios. These findings show the importance of robust interface algorithms in GDRTCS for maintaining high-fidelity simulations despite communication delays. Future work will focus on refining these techniques and exploring their applications in more complex, large-scale power system simulations.

## ACKNOWLEDGMENT

DISTRIBUTION STATEMENT A. Approved for public release; distribution is unlimited. OPSEC8888.

## REFERENCES

[1] E. Buraimoh, G. Ozkan, L. Timilsina, P. K. Chamarthi, B. Papari, and C. S. Edrington, "Overview of interface algorithms, interface signals, communication and delay in real-time co-simulation of distributed power systems," *IEEE Access*, vol. 11, pp. 103925–103955, 2023.

[2] M. Stevic, A. Estebsari, and S. Vogel, "Multi-site European framework for real-time co-simulation of power systems," *IET Gener., Transmiss. Distrib.*, vol. 11, no. 17, pp. 4126–4135, 2017.

[3] S. Thakar, V. Vittal, R. Ayyanar, and C. Rojas, "The impact of detailed distribution system representation in dynamic sub-transmission-distribution co-simulation," *IEEE Open Access J. Power Energy*, vol. 10, pp. 490–502, 2023.

[4] Z. Shen, F. Arraño-Vargas, H. R. Wickramasinghe, and G. Konstantinou, "Development of power system models for distributed real-time simulations," *IEEE Access*, vol. 10, pp. 119706–119721, 2022.

[5] M. R. Nasab, R. Cometa, S. Bruno, G. Giannoccaro, and M. La Scala, "Power systems simulation and analysis: A review on current applications and future trends in DRTS of grid-connected technologies," *IEEE Access*, vol. 12, pp. 121320–121345, 2024.

[6] P. G. Papageorgiou, P. T. Papafilippou, K. O. Oureilidis, and G. C. Christoforidis, "An adaptive controller of a hybrid storage system for power smoothing with enlarged battery lifetime," *IEEE Trans. Sustain. Energy*, vol. 15, no. 4, pp. 2567–2580, Oct. 2024.

[7] M. H. Syed et al., "Real-time coupling of geographically distributed research infrastructures: Taxonomy, overview, and real-world smart grid applications," *IEEE Trans. Smart Grid*, vol. 12, no. 2, pp. 1747–1760, Mar. 2021.

[8] L. Barbierato et al., "Locally distributed digital real-time power system co-simulation via multi-phase distributed transmission line model," *IEEE Trans. Ind. Appl.*, vol. 60, no. 6, pp. 8137–8146, Nov./Dec. 2024.

[9] L. Barbierato et al., "Facilitating smart grids integration through a hybrid multi-model co-simulation framework," *IEEE Access*, vol. 12, pp. 104878–104897, 2024.

[10] R. Liu, M. Mohanpurkar, M. Panwar, R. Hovsapian, A. Srivastava, and S. Suryanarayanan, "Geographically distributed real-time digital simulations using linear prediction," *Int. J. Elect. Power Energy Syst.*, vol. 84, pp. 308–317, 2017.

[11] A. Monti et al., "A global real-time superlab: Enabling high penetration of power electronics in the electric grid," *IEEE Power Electron. Mag.*, vol. 5, no. 3, pp. 35–44, Sep. 2018.

[12] M. Mirz, A. Estebsari, F. Arrigo, E. Bompard, and A. Monti, "Dynamic phasors to enable distributed real-time simulation," in *Proc. 6th Int. Conf. Clean Elect. Power*, 2017, pp. 139–144.

[13] V. Patel et al., "Performance analysis of smart grid communication networks using co-simulation," *IEEE Access*, vol. 12, pp. 164767–164776, 2024.

[14] T. Ersal, M. Brudnak, A. Salvi, J. L. Stein, Z. Filipi, and H. K. Fathy, "Development and model-based transparency analysis of an internet-distributed hardware-in-the-loop simulation platform," *Mechatronics*, vol. 21, no. 1, pp. 22–29, 2011.

[15] X. Liang, M. Talha, J. Pannell, H. Su, and A. Bowes, "A novel OPAL-RT real-time simulator-based experimental approach to study open-switch faults of interfacing inverters of renewable distributed generation in microgrids," *IEEE Trans. Ind. Appl.*, vol. 61, no. 3, pp. 5218–5229, May/Jun. 2025.

[16] N. Kumar, P. Aryan, G. L. Raja, and U. R. Muduli, "Robust frequency-shifting based control amid false data injection attacks for interconnected power systems with communication delay," *IEEE Trans. Ind. Appl.*, vol. 60, no. 2, pp. 3710–3723, Mar./Apr. 2024.

[17] S. Guo, Y. Liu, Y. Zheng, and T. Ersal, "A delay compensation framework for connected testbeds," *IEEE Trans. Syst., Man, Cybern. Syst.*, vol. 52, no. 7, pp. 4163–4176, Jul. 2022.

[18] L. Zhao et al., "Remote driving of road vehicles: A survey of driving feedback, latency, support control, and real applications," *IEEE Trans. Intell. Veh.*, early access, Feb. 06, 2024, doi: 10.1109/TIV.2024.3362597.

[19] L. Barbierato et al., "Exploring stability and accuracy limits of distributed real-time power system simulations via system-of-systems cosimulation," *IEEE Syst. J.*, vol. 17, no. 2, pp. 3354–3365, Jun. 2023.

[20] M. O. Faruque et al., "Real-time simulation technologies for power systems design, testing, and analysis," *IEEE Power Energy Technol. Syst. J.*, vol. 2, no. 2, pp. 63–73, Jun. 2015.

[21] M. Stevic, M. Panwar, M. Mohanpurkar, R. Hovsapian, and A. Monti, "Empirical study of simulation fidelity in geographically distributed real-time simulations," in *Proc. North Amer. Power Symp.*, 2017, pp. 1–6.

[22] J. Rupasinghe, S. Filizadeh, and K. Strunz, "Assessment of dynamic phasor extraction methods for power system co-simulation applications," *Electric Power Syst. Res.*, vol. 197, 2021, Art. no. 107319.

[23] P. J. Koralewicz et al., "Distributed real-time simulation and its applications to wind energy research," National Renewable Energy Lab.(NREL), Golden, CO, USA, Tech. Rep. NREL/CP-5000-72545, 2018.

[24] S. Vogel et al., "Distributed power hardware-in-the-loop testing using a grid-forming converter as power interface," *Energies*, vol. 13, no. 15, 2020, Art. no. 3770.

[25] W. Liu, Z. Zhao, H. Xu, Y. Zeng, and L. Yuan, "Multi-rate co-simulation framework with Taylor-series-based variable-step solver for grid-connected power converters," *Chin. J. Elect. Eng.*, vol. 11, no. 1, pp. 59–73, 2025.

[26] K. Mudunkotuwa and S. Filizadeh, "Co-simulation of electrical networks by interfacing EMT and dynamic-phasor simulators," *Electric Power Syst. Res.*, vol. 163, pp. 423–429, 2018.

[27] T. Yang, S. Bozhko, J.-M. Le-Peuvedic, G. Asher, and C. I. Hill, "Dynamic phasor modeling of multi-generator variable frequency electrical power systems," *IEEE Trans. Power Syst.*, vol. 31, no. 1, pp. 563–571, Jan. 2016.

[28] M. Stevic and A. Monti, "A bilateral teleoperation approach for interface algorithms in distributed real-time simulations," in *Proc. IEEE Workshop Complexity Eng.*, 2018, pp. 1–5.

[29] M. H. Syed, E. Guillo-Sansano, S. M. Blair, A. Avras, and G. M. Burt, "Synchronous reference frame interface for geographically distributed real-time simulations," *IET Gener., Transmiss. Distrib.*, vol. 14, no. 23, pp. 5428–5438, 2020.

[30] S. Vogel et al., "Improvements to the co-simulation interface for geographically distributed real-time simulation," in *Proc. 45th Annu. Conf. IEEE Ind. Electron. Soc.*, 2019, vol. 1, pp. 6655–6662.

[31] M. Stevic, S. Vogel, A. Monti, and S. D'Arco, "Feasibility of geographically distributed real-time simulation of HVDC system interconnected with AC networks," in *Proc. IEEE Eindhoven PowerTech*, 2015, pp. 1–5.

[32] J. D. Lara, R. Henriquez-Auba, D. Ramasubramanian, S. Dhople, D. S. Callaway, and S. Sanders, "Revisiting power systems time-domain simulation methods and models," *IEEE Trans. Power Syst.*, vol. 39, no. 2, pp. 2421–2437, Mar. 2024.

[33] E. G. Sansano, "Novel methods for enhancing accuracy and stability of power hardware-in-the-loop simulations," Ph.D. dissertation, Dept. of Electronic and Electrical Eng., Univ. of Strathclyde, Glasgow, U.K., 2018. [Online]. Available: https://doi.org/10.48730/7zb9-nb64

[34] J. Wen, L. Jiang, Y. Chen, C.-C. Chu, J. Zhu, and Z. Qiu, "Design of data distributed service-based distributed co-simulation platform of power systems," *IEEE Trans. Ind. Appl.*, vol. 60, no. 6, pp. 8115–8127, Nov./Dec. 2024.

[35] E. Bompard et al., "Latency and simulation stability in a remote power hardware-in-the-loop cosimulation testbed," *IEEE Trans. Ind. Appl.*, vol. 57, no. 4, pp. 3463–3473, Jul./Aug. 2021.

[36] J. C. Junior, M. Balza, S. N. Silva, L. M. da Silva, and M. A. Fernandes, "Optimizing tactile feedback devices with fixed-point computation on FPGA," *Circuits, Syst., Signal Process.*, vol. 44, pp. 3826–3864, 2025.

[37] R. Brandl, "Operational range of several interface algorithms for different power hardware-in-the-loop setups," *Energies*, vol. 10, no. 12, 2017, Art. no. 1946.

[38] E. Buraimoh et al., "Model free time delay compensation for damped impedance method interfaced power system co-simulation testing," SAE Tech. Papers, Tech. Rep. 2023-01-1600, 2023, Accessed: Jun. 5, 2024. [Online]. Available: https://www.sae.org/publications/technical-papers/content/2023-01-1600/

[39] Y. Zheng et al., "A predictor-based framework for delay compensation in networked closed-loop systems," *IEEE/ASME Trans. Mechatron.*, vol. 23, no. 5, pp. 2482–2493, Oct. 2018.

[40] S. Sadjina and E. Pedersen, "Energy conservation and coupling error reduction in non-iterative co-simulations," *Eng. Comput.*, vol. 36, pp. 1579–1587, 2020.

[41] V. Paduani et al., "A real-time T&D co-simulation platform for testing grid services of distributed energy resources," *IEEE Access*, vol. 12, pp. 142394–142405, 2024.